Supplementary Information for

Robust ferroelectricity in HfO_2-based bulk crystals via polymorphic engineering

Shuxian Wang[1], Yihao Shen[1], Xiaoyu Yang[2], Pengfei Nan[2], Haohai Yu[1]*, Binghui Ge[2]*, Shujun Zhang[3]* & Huaijin Zhang[1]*

[1]State Key Laboratory of Crystal Materials and School of Crystal Materials, Shandong University, Jinan, China.

[2]Information Materials and Intelligent Sensing Laboratory of Anhui Province, Institutes of Physical Science and Information Technology, Anhui University, Hefei, China.

[3]Institute for Superconducting and Electronic Materials, Australian Institute of Innovative Materials, University of Wollongong, Wollongong, Australia.

*Corresponding author. Email: haohaiyu@sdu.edu.cn (H.Y.); bhge@ahu.edu.cn (B.G.); shujun@uow.edu.au (S.Z.); huaijinzhang@sdu.edu.cn (H.Z.)

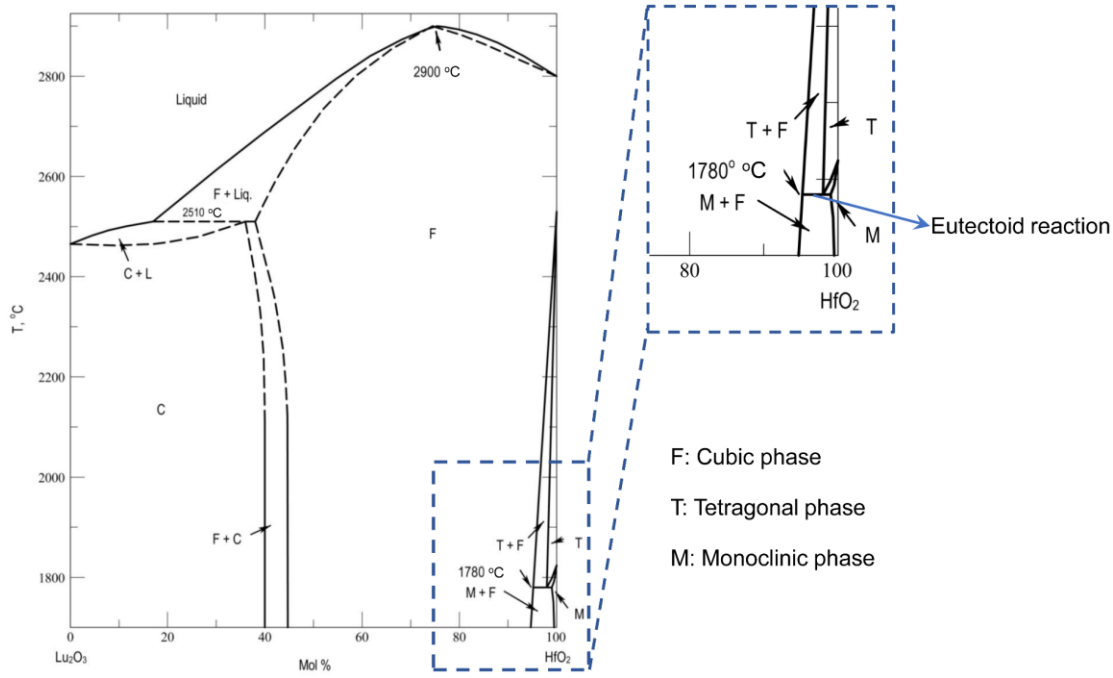

Supplementary Fig. 1. Lu_2O_3-HfO_2 phase diagram. The inset is the magnified Lu_2O_3-HfO_2 phase diagram near pure HfO_2. The eutectoid reaction denotes the phase transition from the tetragonal phase to the cubic and monoclinic phases. The phase diagram is from the National Institute of Standards and Technology (NIST) library.

Supplementary Note 1

For the crystal growth of HfO_2-based crystals, the consideration of relevant phase diagrams is indispensable. The pure HfO_2 specimen from the high-temperature melt (~2800°C) to room temperature would undergo two phase transitions ($c \rightarrow t$ and $t \rightarrow m$), and hence only the *m* phase can be obtained at room temperature. As for the RE_2O_3-HfO_2 binary systems, the RE^{3+} ions with larger ionic radii usually result in the $RE_2Hf_2O_7$ phase even if in the phase component near the pure HfO_2 phase (such as La^{3+}, Pr^{3+}, Nd^{3+}, and Sm^{3+} ions). Thus, only the introduction of smaller RE^{3+} ions is a feasible way to realize the stabilization of metastable phases in the crystal growth of bulk crystals. As Supplementary fig. 1 and Table S1 demonstrate, to avoid the bulk crystals without the *m* phase, the eutectoid reaction at ~1780°C ($t \rightarrow c + m$) is necessary to be considered. Combined with the obtained XRD results shown in Supplementary figs. 2-5, such a selection rule is further ascertained.

Besides, most of the previous studies deemed that the phase evolution in RE:HfO_2 mainly originates from the generation of oxygen vacancies from the heterovalent substitution, especially for the existence of ferroelectricity in the o-FE phase. Hence, the Lu:HfO_2 (5 and 10.5 at. %) and Ta,Lu:HfO_2 (5-10.5 at. %) crystals were grown to analyze the modulation effect of oxygen vacancies. Lu^{3+} showed a lower ionic valence state than that of Hf^{4+}, giving rise to oxygen vacancies in the crystal lattice to maintain charge neutrality in the host. However, Ta^{5+} ions neutralized the oxygen vacancies derived from the introduction of RE^{3+} ions and might influence the phase composition in the bulk crystal. As shown in Supplementary fig. 2, The XRD data of Ta,Lu:HfO_2 (5-10.5 at. %) is similar to that of Lu:HfO_2 (5 at. %), but is different from that of Lu:HfO_2 (10.5 at. %). Such a result indicates that the phase evolution of the RE:HfO_2 crystals is closely correlated to the content of oxygen vacancies stemming from the heterovalent substitution.

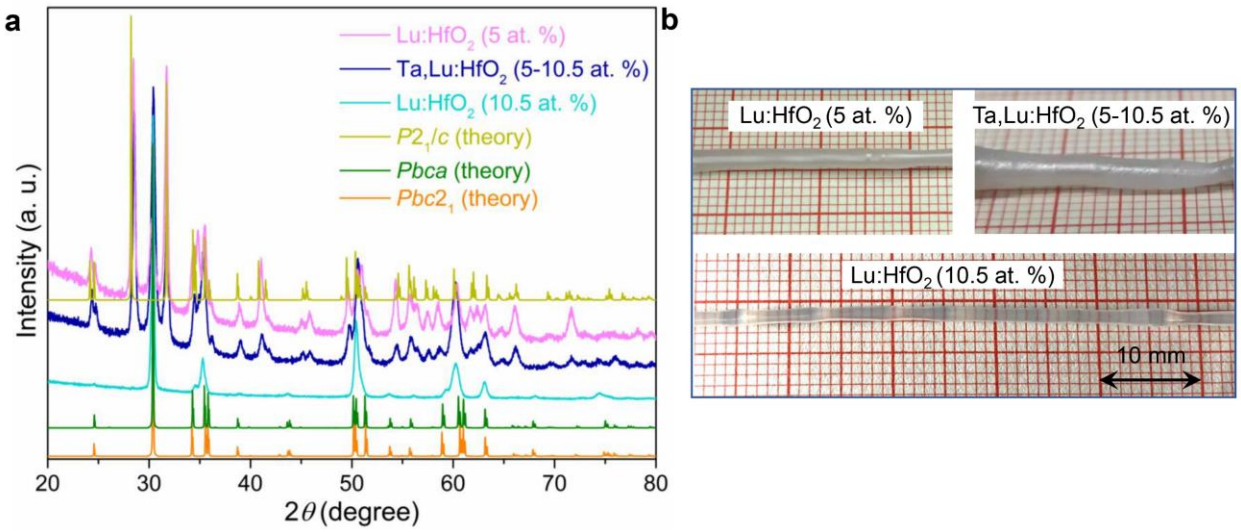

Supplementary Fig. 2. a, Room-temperature XRD data of the Lu:HfO_2 (5 at. % and 10.5 at. %) and Ta,Lu:HfO_2 (5-10.5 at. %) bulk crystals. **b**, The related crystal photographs. The standard cards of the $P2_1/c$ and *Pbca* phases correspond to ICSD Nos. 173964 and 79913, respectively, and the standard one of the $Pbc2_1$ phase is from Ref. [*Phys. Rev. Lett.* 125, 257603 (2020)].

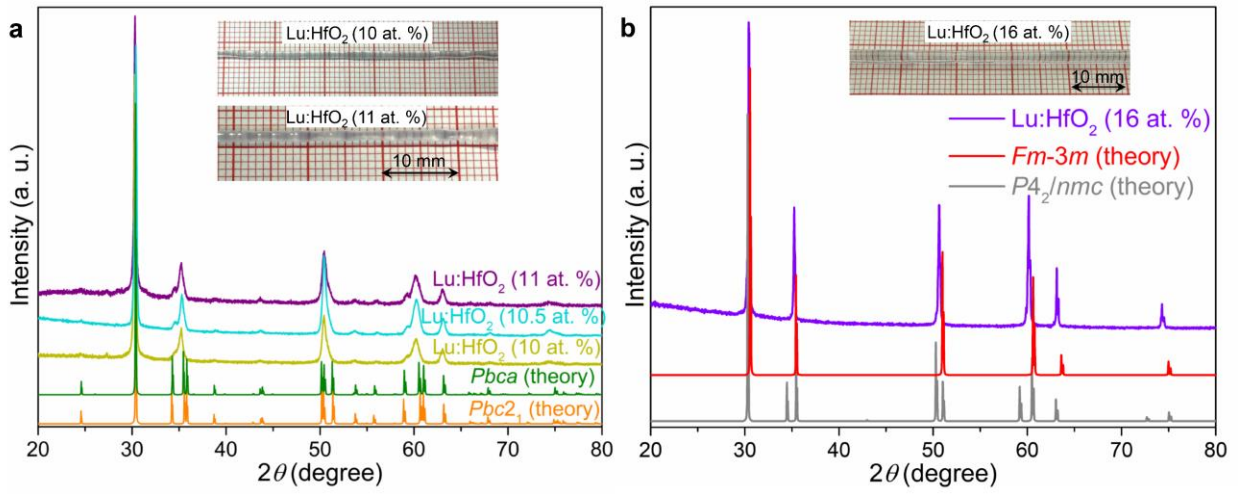

Supplementary Fig. 3. Room-temperature XRD data of the Lu:HfO_2 bulk crystals with different Lu doping concentrations. a, For 10, 10.5, and 11 at. %. **b**, For 16 at. %. The inset denotes the related crystal photographs.

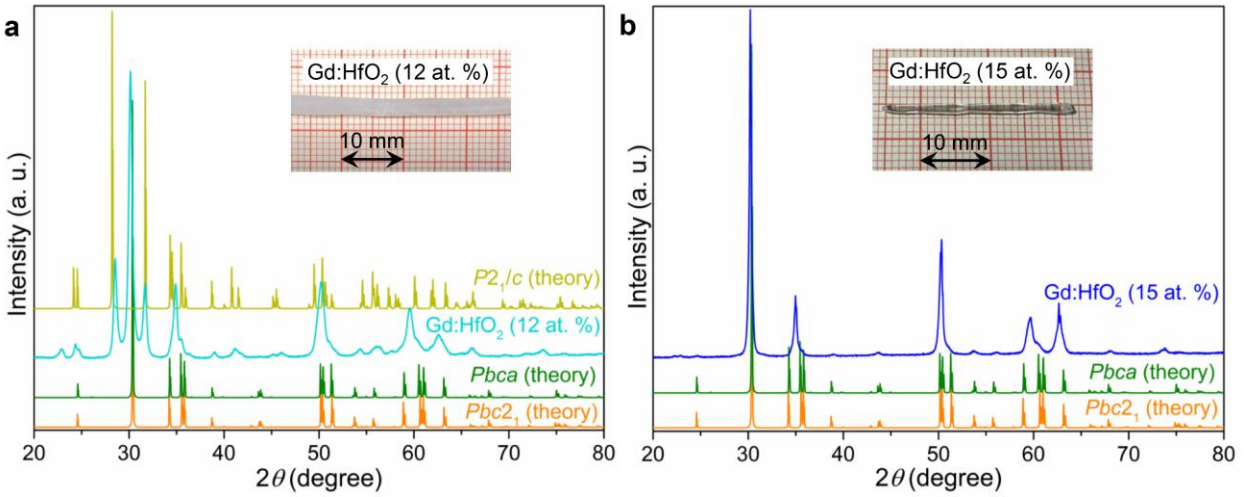

Supplementary Fig. 4. Room-temperature XRD results and crystal photographs (the inset) of the Gd:HfO_2 (12 and 15 at. %) specimens.

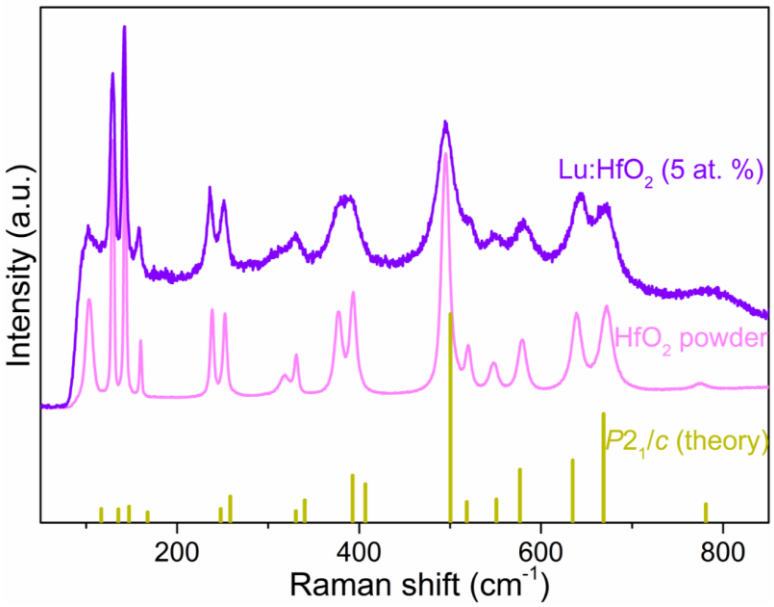

Supplementary Fig. 5. Room-temperature Raman spectra of the Lu:HfO_2 crystal (5 at. %) and HfO_2 raw powder. The theoretical Raman vibrational modes of the $P2_1/c$ phases are from Ref. [*npj Quantum Mater.* 7, 32 (2022)].

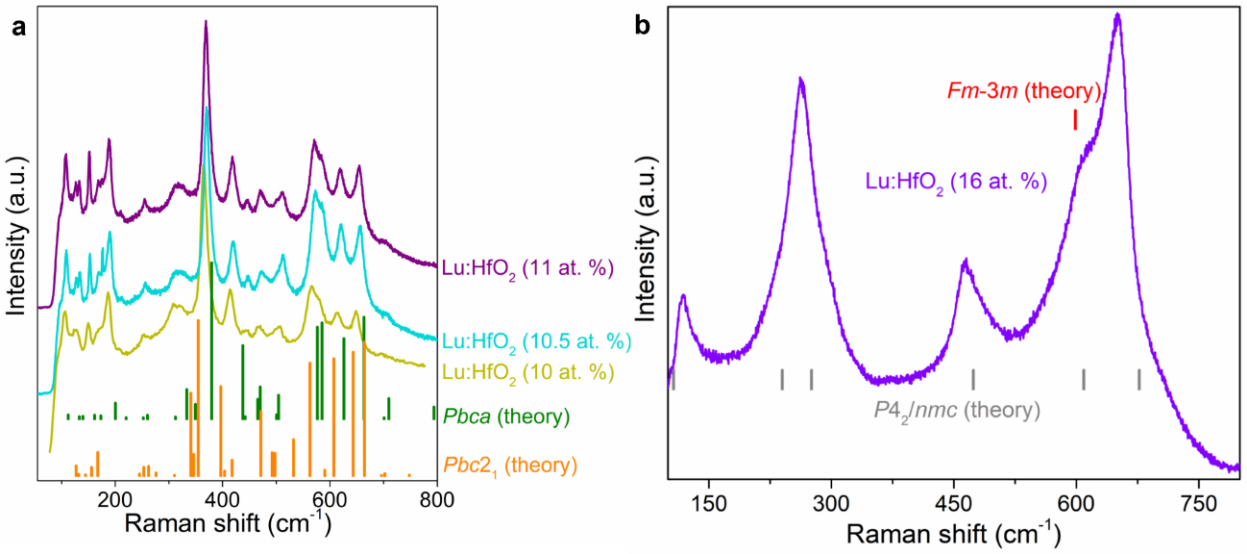

Supplementary Fig. 6. Room-temperature Raman spectra of the Lu:HfO_2 crystals. The theoretical Raman vibrational modes of the *Pbca*, $Pbc2_1$, $P4_2/nmc$, and *Fm*-3*m* phases are from Ref. [*npj Quantum Mater.* 7, 32 (2022)].

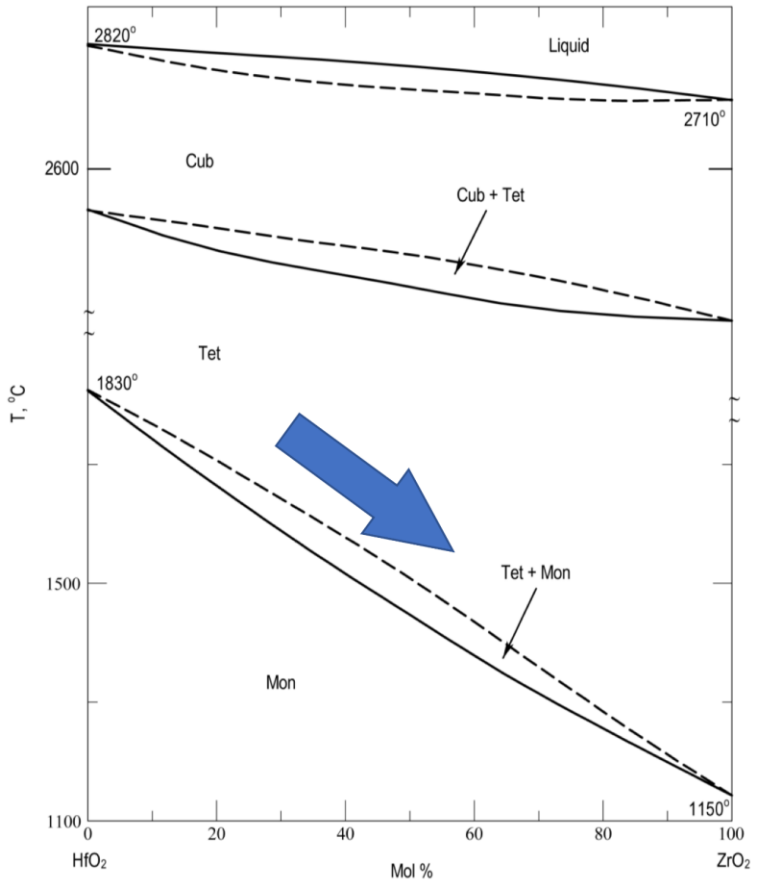

Supplementary Fig. 7. ZrO_2-HfO_2 phase diagram (No. 09365). Along with the increase in Zr doping concentration, the *t-m* transition temperature shows a gradual decline tendency.

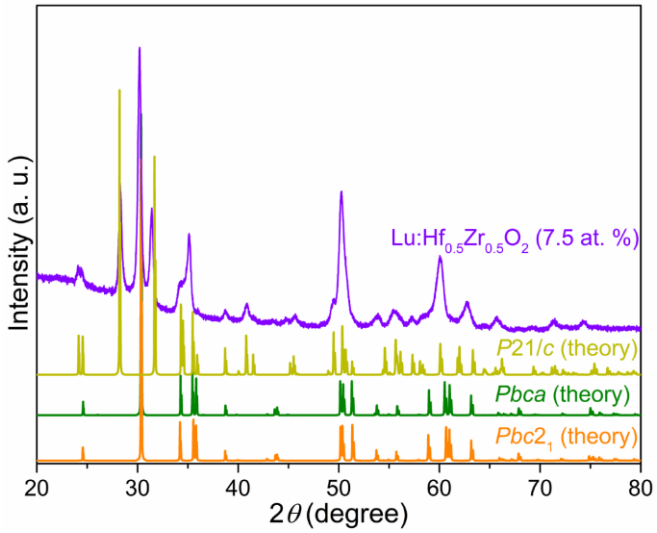

Supplementary Fig. 8. Room-temperature XRD result of the $Lu:Hf_{0.5}Zr_{0.5}O_2$ (7.5 at. %) bulk crystal. When the Lu doping concentration was below the C_{RE} value (~9.18 at. %), the *m* phase could be observed in the final bulk crystal, agreeing with those in $Lu:HfO_2$ crystals.

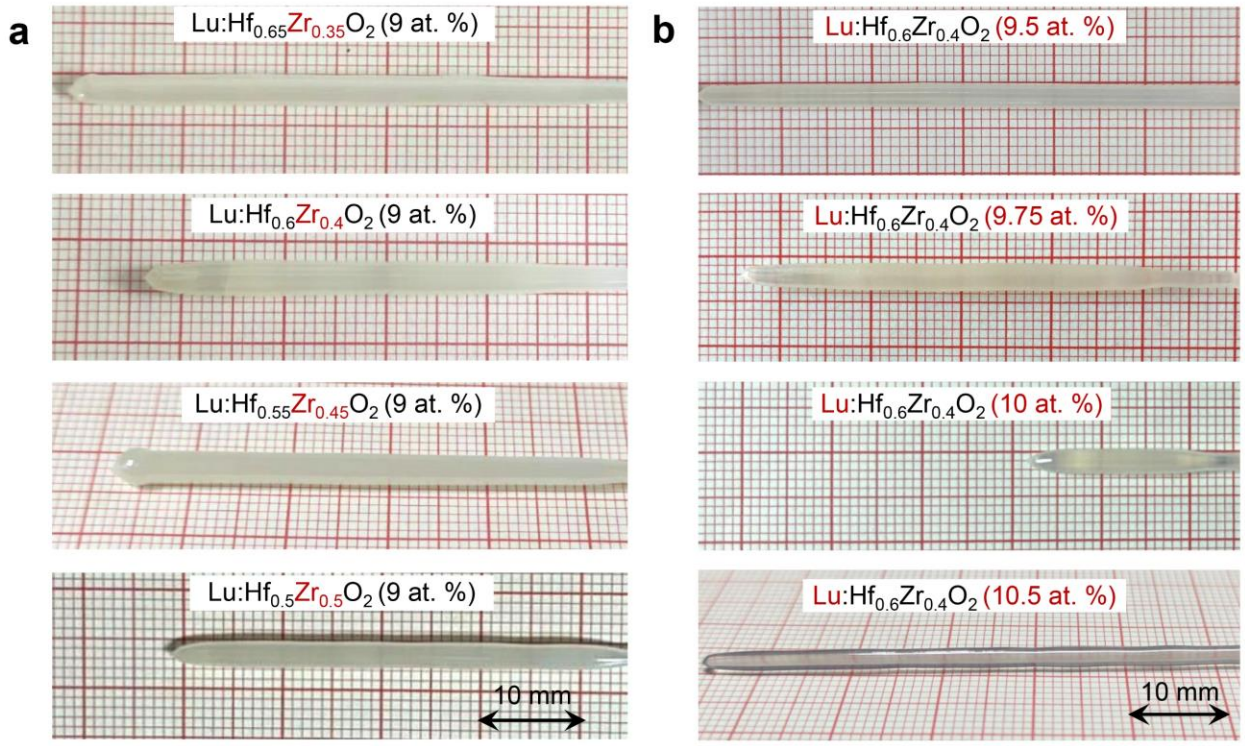

Supplementary Fig. 9. Photographs of several as-grown Lu:$Hf_{1-x}Zr_xO_2$ bulk crystals.

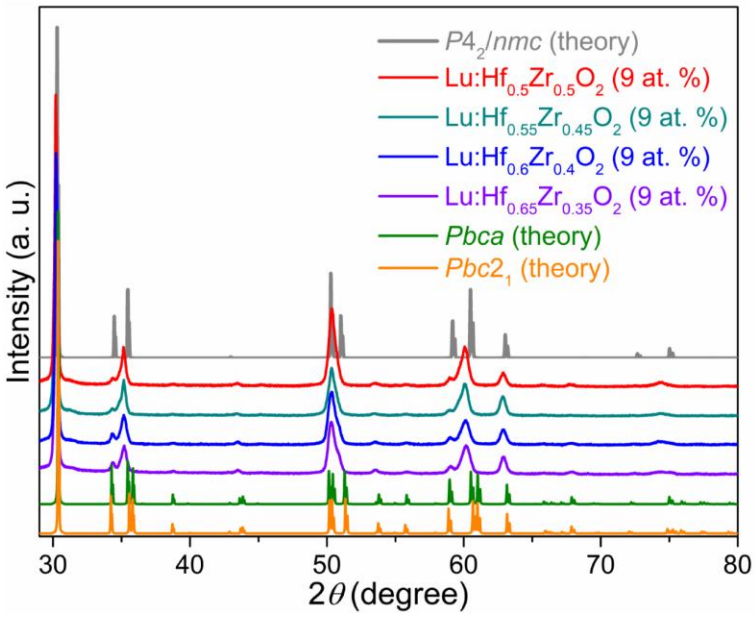

Supplementary Fig. 10. Room-temperature XRD data of the Lu:$Hf_{1-x}Zr_xO_2$ crystal specimens. The Lu doping concentration was fixed at 9 at. %. Even if the Zr doping concentration was altered from 35 to 50 at. %, the *o* phase could be clearly observed in the as-grown bulk crystals.

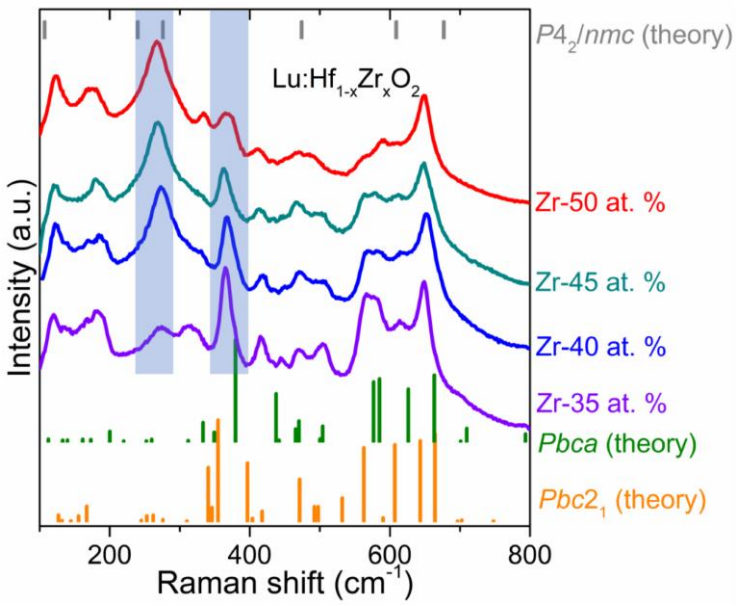

Supplementary Fig. 11. Room-temperature Raman spectra of the Lu:$Hf_{1-x}Zr_xO_2$ samples. The Lu doping concentration was fixed at 9 at. %. With the increase in Zr doping content, the Raman vibrations of the *t* phase gradually became more obvious compared to that of the *o* phase.

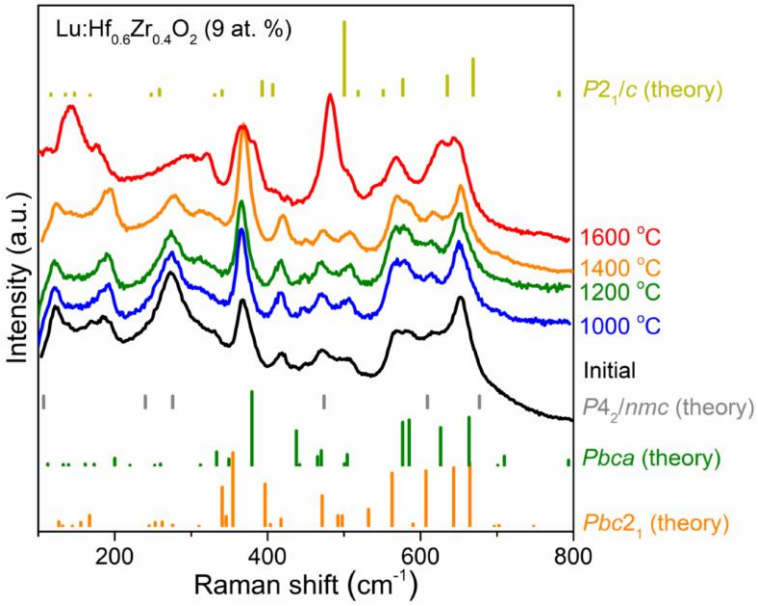

Supplementary Fig. 12. Room-temperature Raman spectra of the Lu:$Hf_{0.6}Zr_{0.4}O_2$ (9 at. %) sample under different annealing temperatures. All the annealing processes were conducted under the air atmosphere. The rise in annealing temperature accelerated the *t-o* phase transition. When the temperature reached 1600°C, the vibrational modes of the *m* phase could be clearly observed, being consistent with the obtained result in the Y:HfO_2 bulk crystal [*Nat. Mater.* 20, 826-832 (2021)].

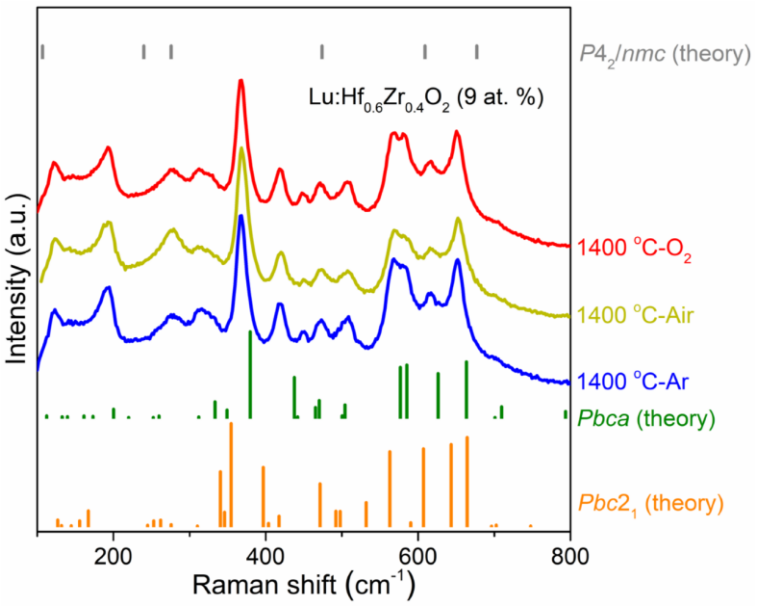

Supplementary Fig. 13. Room-temperature Raman spectra of the Lu:$Hf_{0.6}Zr_{0.4}O_2$ (9 at. %) sample under different annealing atmospheres. The annealing temperature was 1400°C. The change of atmosphere almost does not influence the *t-o* phase transformation. Such a result means that the phase control in Lu:$Hf_{1-x}Zr_xO_2$ is realized by the large chemical pressure caused by the cation substitution (for coordination number (CN) = 8, the ionic radii of Hf^{4+}, Zr^{4+}, and Lu^{3+} correspond to 0.83, 0.84, and 0.977 Å, respectively). High-temperature annealing leads to the related cation diffusion and gives rise to the *t-o* (or *t-m*) phase transformation owing to the energetically favorable property [*Nat. Mater*. 20, 826-832 (2021)].

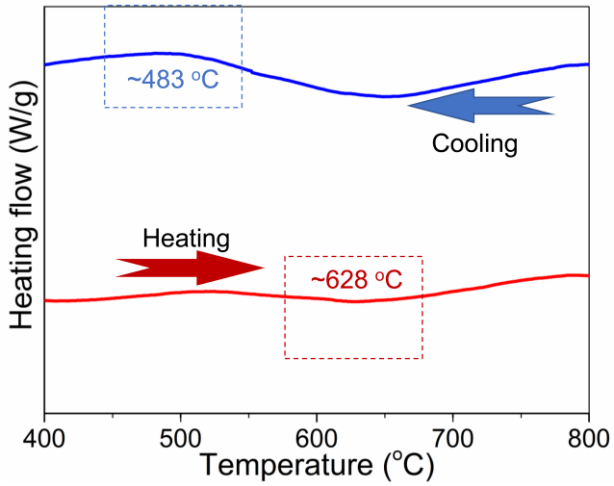

Supplementary Fig. 14. DSC curves of the Lu:$Hf_{0.6}Zr_{0.4}O_2$ (9.25 at. %) sample. The endothermic peak in the heating process was located at ~628°C, while the exothermic peak in the cooling process was centered at ~483°C.

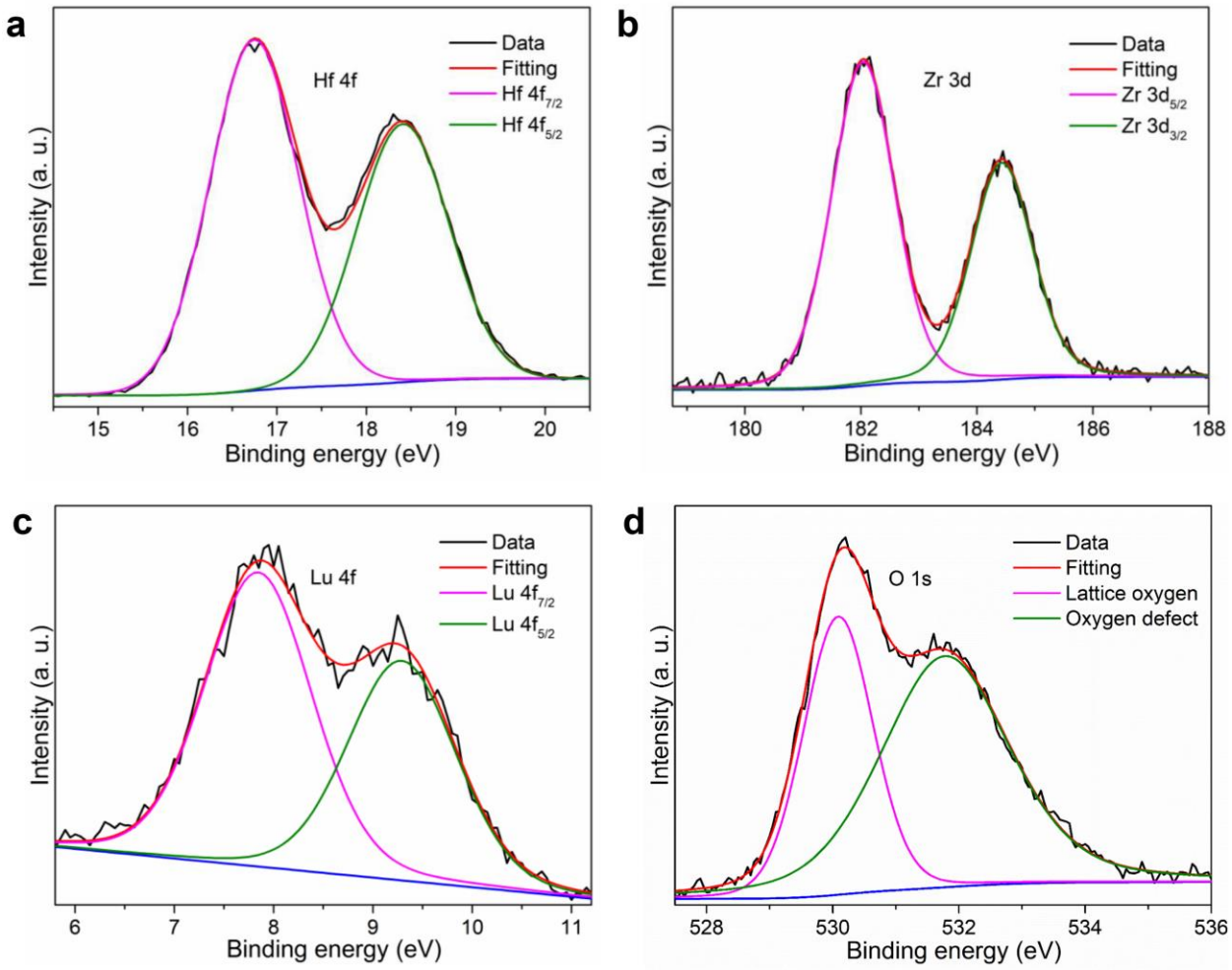

Supplementary Fig. 15. High-resolution Hf 4f, Zr 3d, Lu 4f, and O1s XPS spectra of the Lu:$Hf_{0.6}Zr_{0.4}O_2$ (9 at. %) sample. The spin-orbit splittings of elemental Hf, Zr, and Lu were clearly observed. The oxygen defect was also seen owing to the heterovalent ion substitution by the rear-earth ions.

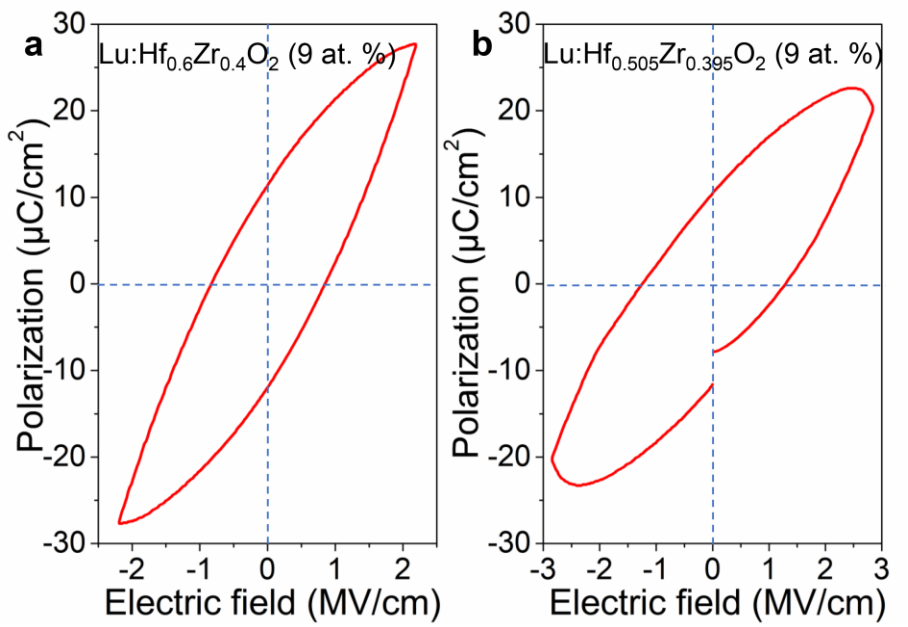

Supplementary Fig. 16. E-P characterizations of several Lu:$Hf_{1-x}Zr_xO_2$ bulk crystals. a, 19-μm-thick Lu:$Hf_{0.6}Zr_{0.4}O_2$ (9 at. %) sample with a P_r value of 11.2 μC/cm^2. **b**, 17-μm-thick Lu:$Hf_{0.505}Zr_{0.395}O_2$ (9 at. %) sample with a P_r value of 10.3 μC/cm^2.

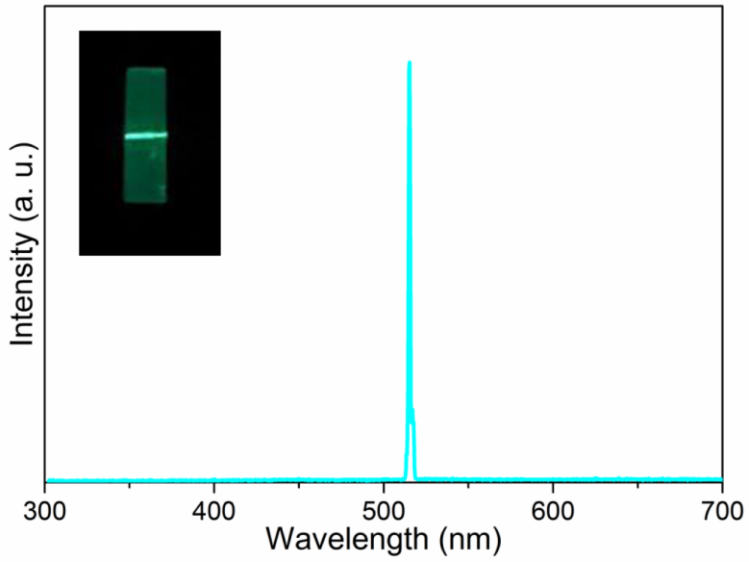

Supplementary Fig. 17. Room-temperature SHG spectrum and image of the Lu:$Hf_{0.6}Zr_{0.4}O_2$ (9 at. %) bulk crystal. The fundamental frequency wavelength was 1030 nm.

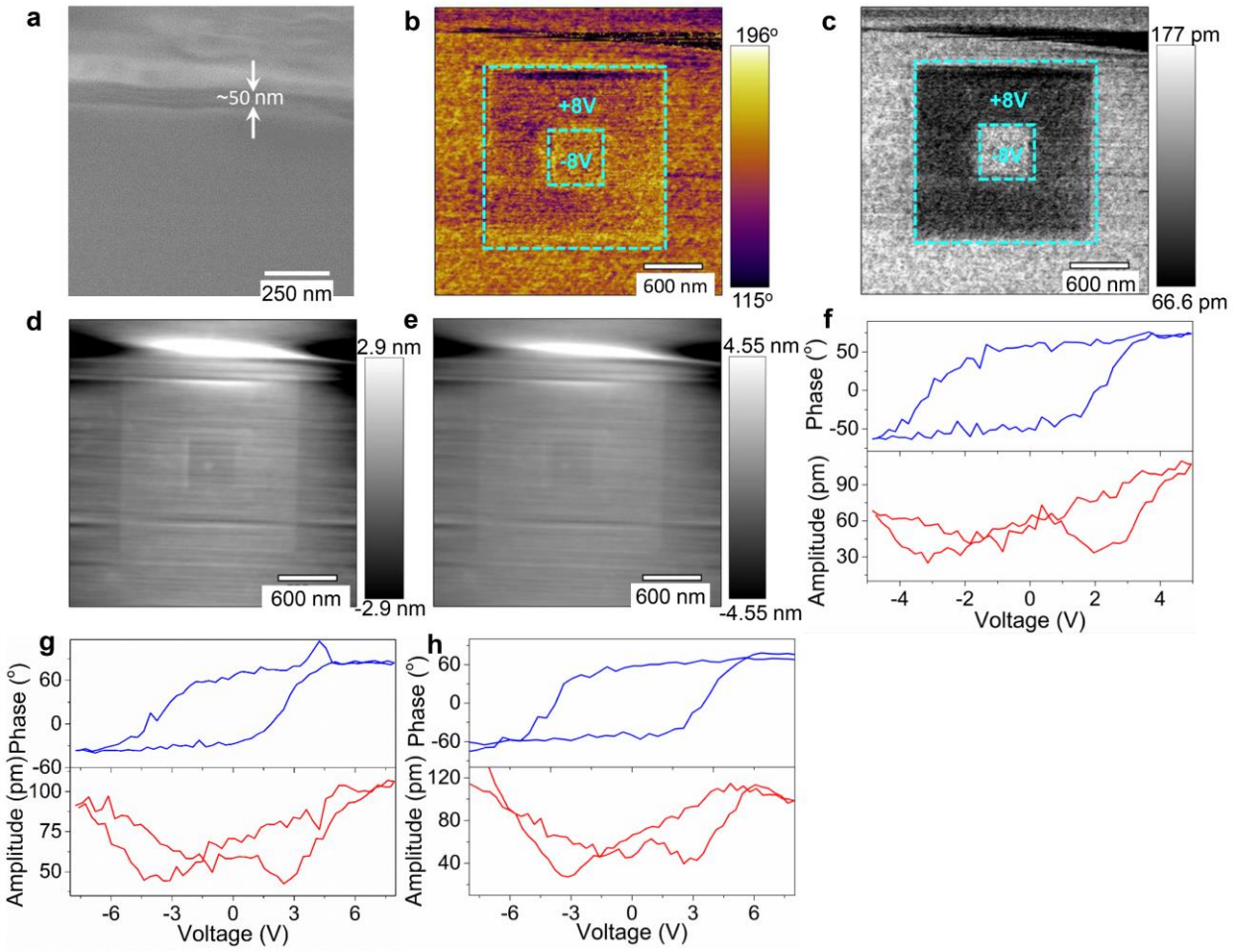

Supplementary Fig. 18. SEM and PFM data of the Lu:$Hf_{0.6}Zr_{0.4}O_2$ (9.25 at. %) sample. a, SEM image. The sample thickness was reduced to ~50 nm via the FIB method. **b-d**, Local PFM phase contrast, amplitude variation, and topography map under different voltages (8 V and -8 V). **e**, Topography map under 10 V and -10 V. **f-h**, Voltage-dependent switching loops of phase and amplitude at different positions.

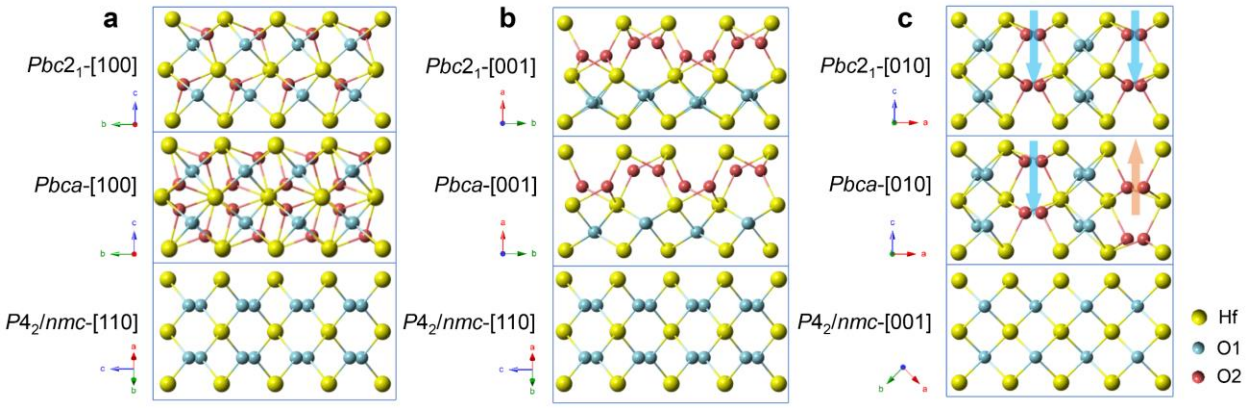

Supplementary Fig. 19. Crystal structures of the different polymorphs of HfO_2, including the *t* (*P*4$_2$/*nmc*), *o*-FE (*Pbc*2$_1$), and *o*-AFE (*Pbca*) phases. The two orthorhombic phases show a similar atomic arrangement along the *c*-axis direction but demonstrate the complex distributions of O atoms along the *a*-axis direction. The observation along the *b*-axis direction of the orthorhombic phases (or the *c*-axis direction of the *t* phase) is beneficial for phase identification. It not only can show the polarization difference between the *o*-FE and *o*-AFE phases but also manifests the displacement discrepancy of O atoms between the *t* and *o* phases.

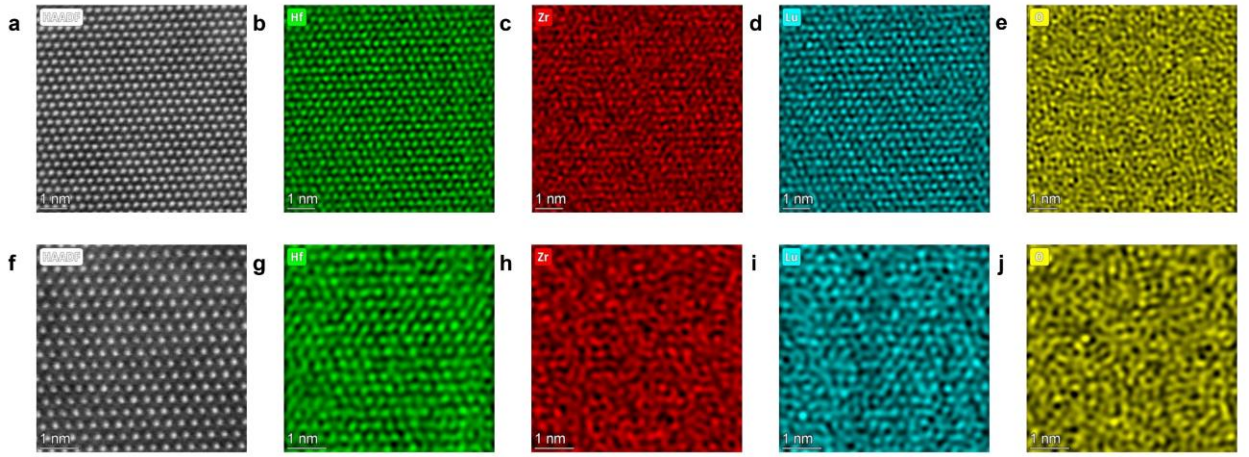

Supplementary Fig. 20. a,**f**, STEM high-angle annular dark-field (HAADF) images of the Lu:$Hf_{0.6}Zr_{0.4}O_2$ (9.25 at. %) sample. The cationic sites could be seen under the HAADF mode. **b**,**g**, STEM-EDS images of elemental Hf. **c**,**h**, STEM-EDS images of elemental Zr. **d**,**i**, STEM-EDS images of elemental Lu. **e**,**j**, STEM-EDS images of elemental O. From the STEM-EDS characterization, we found that elemental O exhibited an evident local inhomogeneous distribution, which is mainly ascribed to the oxygen defects originating from the heterovalent ion substitution.

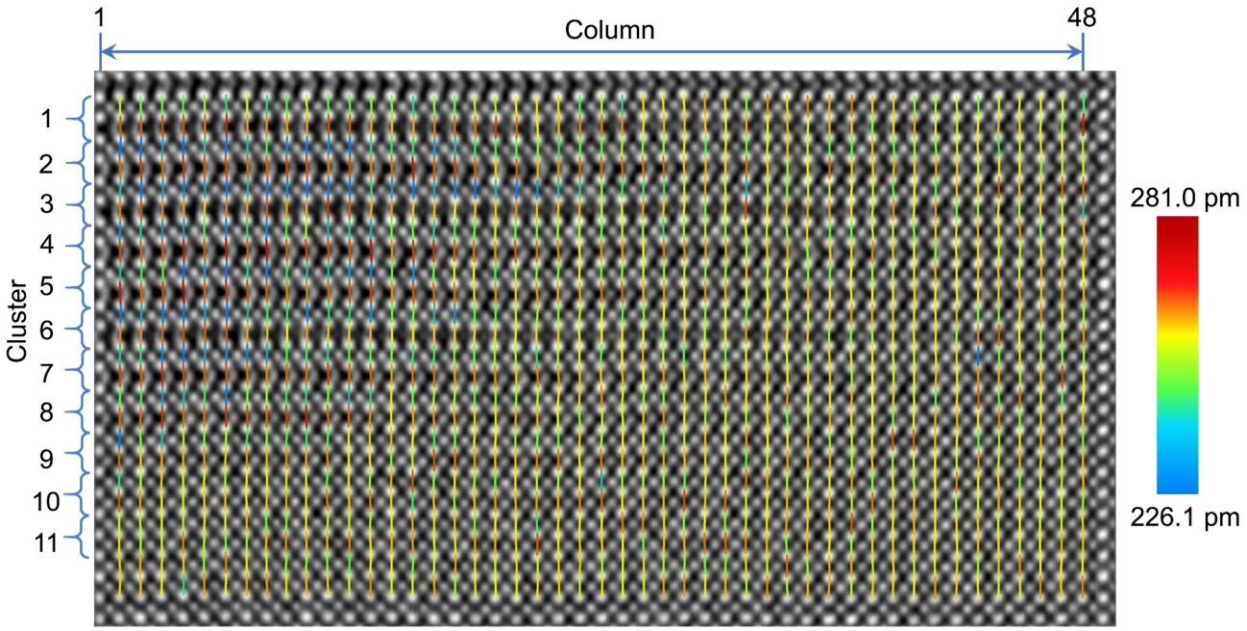

Supplementary Fig. 21. iDPC-STEM image including the *t* (*P*4$_2$/*nmc*), transient (*t*' and *t*"), *o*-FE (*Pbc*2$_1$), and *o*-AFE (*Pbca*) phases. An apparent vertical Hf-Hf distance difference between the polarization and spacer layers (d_1 and d_2) was observed within the *o* phases. By contrast, the distance difference between d_1 and d_2 was not obvious within the *t* phase.

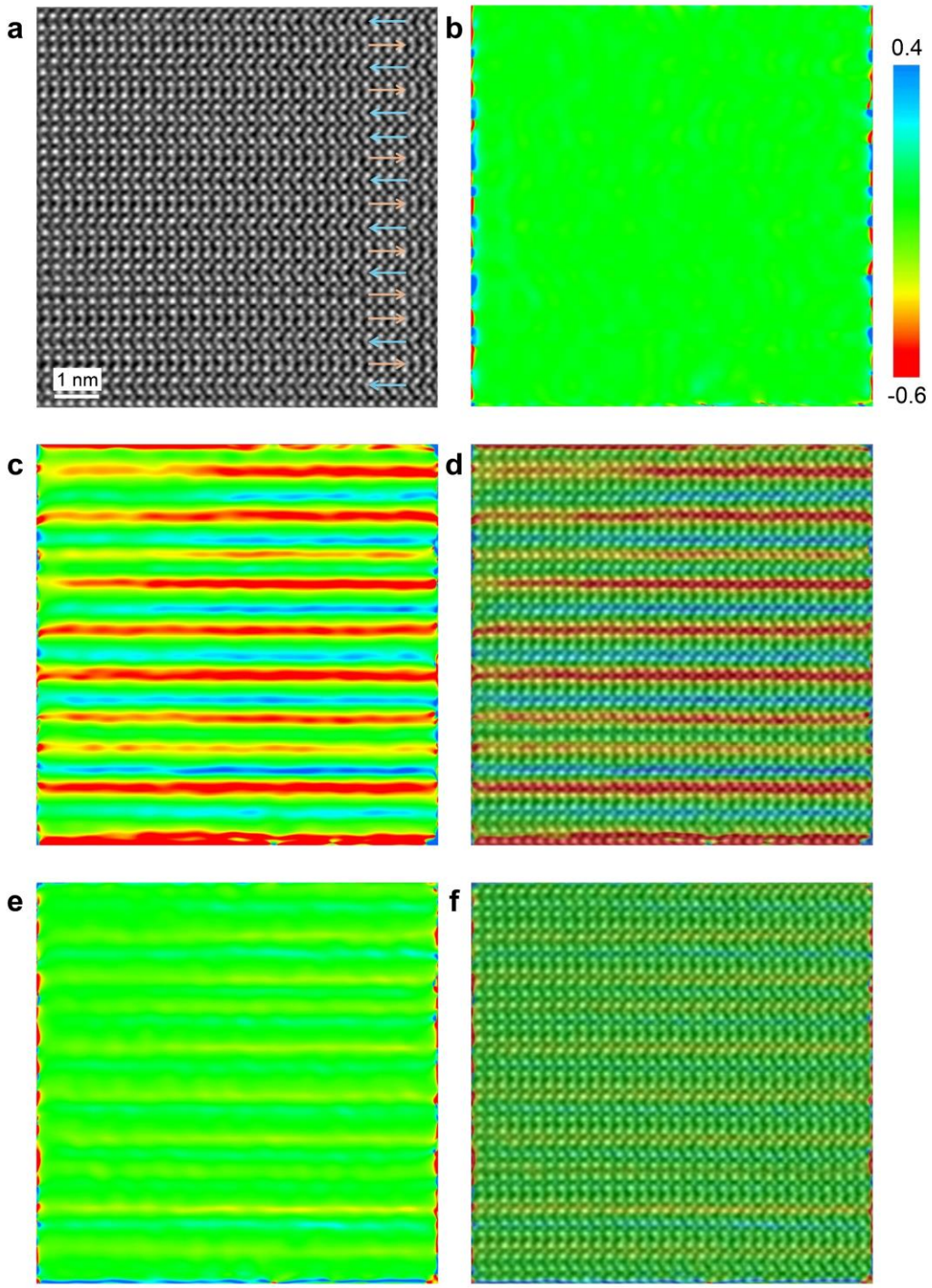

Supplementary Fig. 22. GPA analysis of the Lu:$Hf_{0.6}Zr_{0.4}O_2$ (9.25 at. %) sample including the *o*-FE (*Pbc*2_1) and *o*-AFE (*Pbca*) phases. a, As-measured iDPC-STEM image. **b**, ε_{xx} (normal strain) mapping. *x* and *y* denote the horizontal and vertical coordinates, respectively. **c**, ε_{yy} (normal strain) mapping. **d**, Overlapping profile of the iDPC-STEM and ε_{yy} images. **e**, ε_{xy} (shear strain) mapping. **f**, Overlapping profile of the iDPC-STEM and ε_{xy} images.

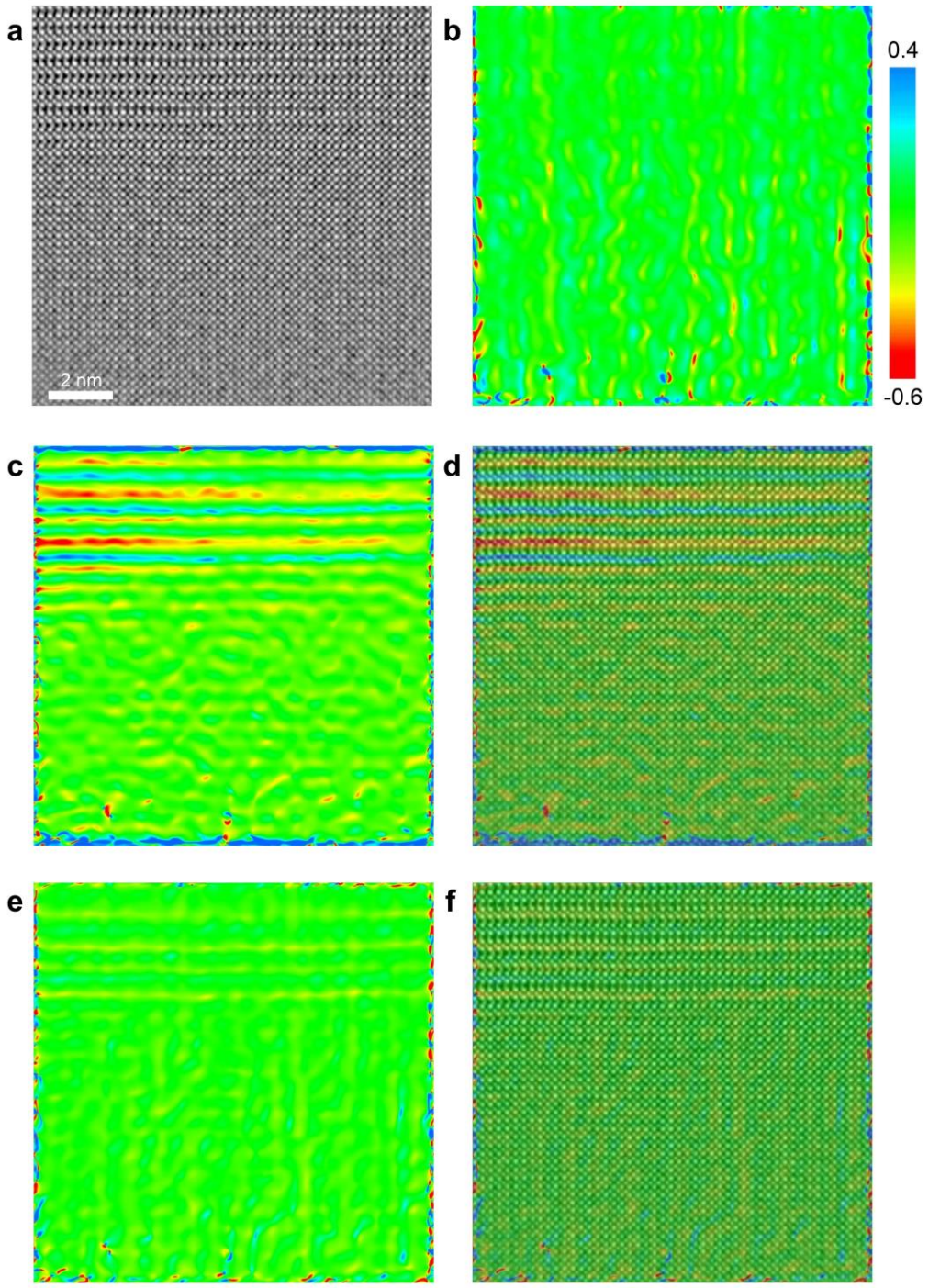

Supplementary Fig. 23. GPA analysis of the Lu:$Hf_{0.6}Zr_{0.4}O_2$ (9.25 at. %) sample with the phase transformation from the *t* phase to the *o*-FE (*Pbc*2_1) or *o*-AFE (*Pbca*) phases. a, As-measured iDPC-STEM image. **b**, ε_{xx} (normal strain) mapping. *x* and *y* denote the horizontal and vertical coordinates, respectively. **c**, ε_{yy} (normal strain) mapping. **d**, Overlapping profile of the iDPC-STEM and ε_{yy} images. **e**, ε_{xy} (shear strain) mapping. **f**, Overlapping profile of the iDPC-STEM and ε_{xy} images.

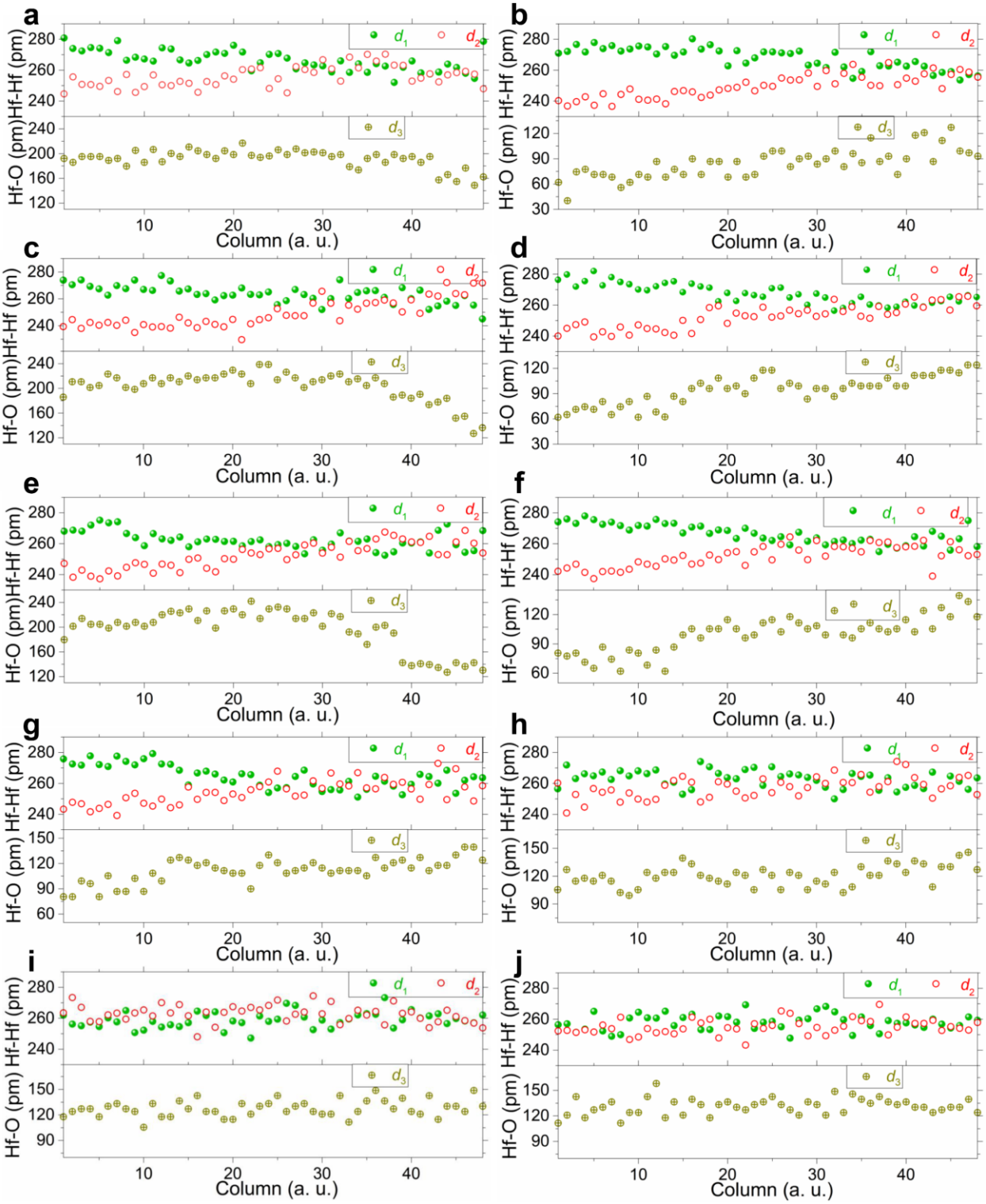

Supplementary Fig. 24. Vertical Hf-Hf (d_1 and d_2) and horizontal Hf-O (d_3) distances in different groups of the iDPC-STEM image shown in Fig. 4 and Supplementary fig. 21. a, For Cluster 1. **b**, For Cluster 2. **c**, For Cluster 3. **d**, For Cluster 5. **e**, For Cluster 6. **f**, For Cluster 7. **g**, For Cluster 8. **h**, For Cluster 9. **i**, For Cluster 10. **j**, For Cluster 11. As shown in Fig. 4, the shift of

the O column toward the left and right sides would result in the decreasing and increasing tendencies of d_3, respectively. According to the changes of d_1, d_2, and d_3, the *t* ($P4_2/nmc$), transient (*t*' and *t*"), *o*-FE ($Pbc2_1$), and *o*-AFE (*Pbca*) phases could be clearly distinguished. In the *t* region (Clusters 10 and 11), d_1, d_2, and d_3 almost showed no obvious difference among different columns, demonstrating a typical *t*-phase structure nature. In the *t*' section (Clusters 1-9), d_3 demonstrated an apparent variation but d_1 was generally consistent with d_2. By comparison, in the *t*" region (Clusters 1-9), an evident change of d_1 and d_2 was observed while the alteration of d_3 was not obvious. In the *o*-FE and *o*-AFE sections (Clusters 1-8), d_1 maintained a ~30 pm value larger than that of d_2, and d_3 almost showed no change.

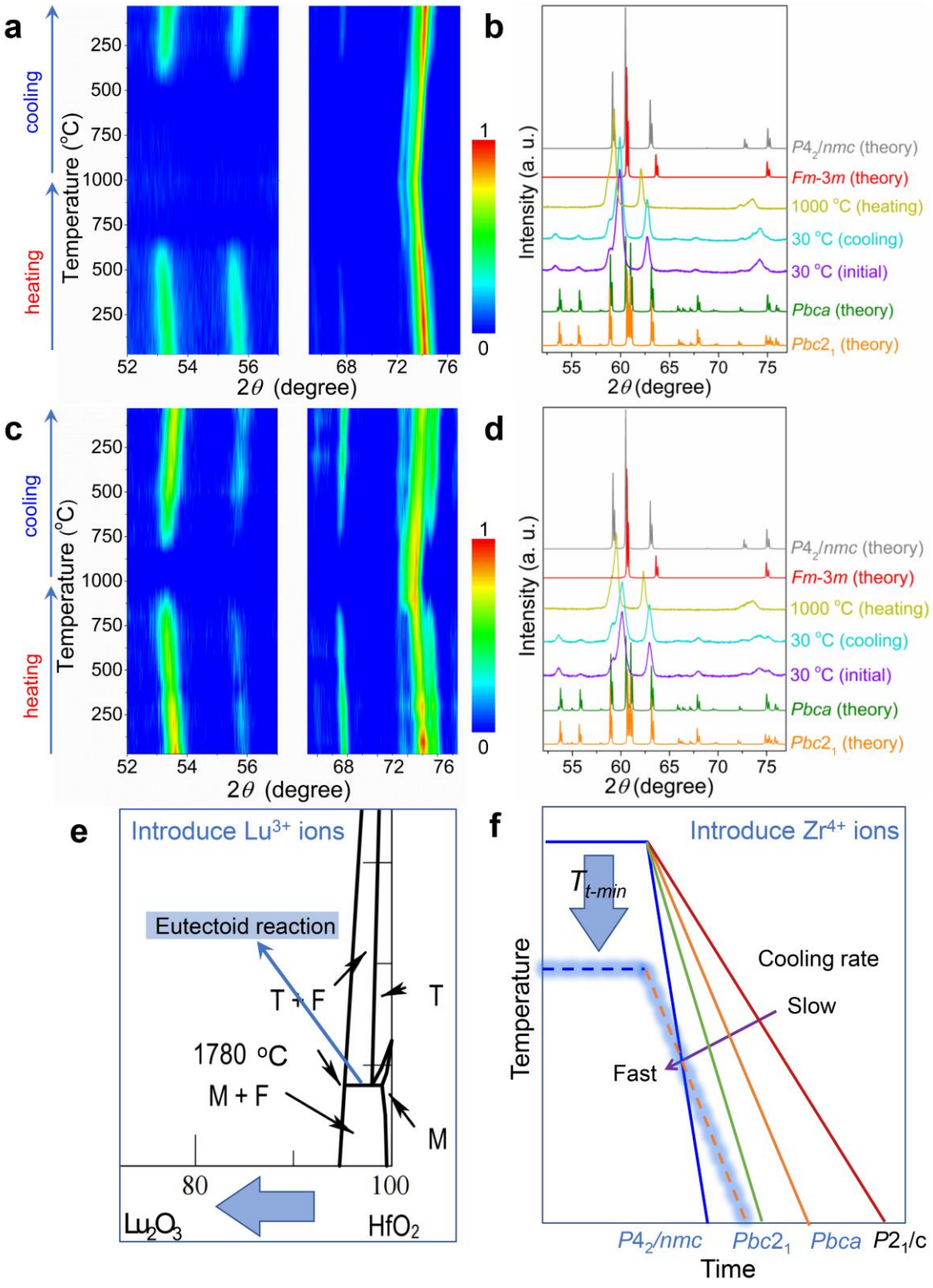

Supplementary Fig. 25. Temperature-dependent structural analysis and phase control mechanism of the Lu:$Hf_{1-x}Zr_xO_2$ and Lu:HfO_2 bulk crystals. a,**b**, Temperature-dependent XRD data of the Lu:$Hf_{0.6}Zr_{0.4}O_2$ (10 at. %) sample from 30 to 1000ºC. The transformation

temperatures in the heating and cooling processes were located at 600-700°C and 400-500°C, respectively. **c**,**d**, Temperature-dependent XRD data of the Lu:HfO_2 (10 at. %) sample from 30 to 1000°C. The transformation temperatures in the heating and cooling processes were located at 800-900°C and 700-800°C, respectively. **e**, Partial Lu_2O_3-HfO_2 phase diagram near pure HfO_2. The eutectoid reaction ($t \rightarrow c + m$) could be avoided by adjusting the Lu doping concentration. **f**, the manipulation of phase transformation from the *t* metastable phase.

Supplementary Note 2

In general, when the quenching rate is slow enough, the $t \rightarrow m$ phase transition is more likely to occur due to the minimum formation energy of the *m* phase. Along with the rise in cooling rate, the *o*-AFE and *o*-FE phases can be stabilized to room temperature. Provided the cooling rate is fast enough, the *t* phase might be directly achieved in the final specimen. In this study, we selected another adjustment pathway to control the phase composition of the Lu:$Hf_{1-x}Zr_xO_2$ bulk crystals. By introducing the Zr^{4+} ions, the minimum stabilization temperature ($T_{t\text{-}min}$) of the *t* phase could be effectively reduced. The related temperature-dependent XRD characterizations further verified that deduction. When the cooling rate was fixed (under the same growth process), reducing the $T_{t\text{-}min}$ value would decrease the transformation time of the *t* phase from $T_{t\text{-}min}$ to room temperature. Such a strategy could bring the metastable phases with larger formation energies to room temperature. The primary phase in the Lu:HfO_2 (10 at. %) bulk crystal was the *o*-AFE phase (Supplementary fig. 6). By contrast, the *t* phase could be also clearly observed in the Lu:$Hf_{0.6}Zr_{0.4}O_2$ (10 at. %) crystal apart from the *o*-AFE phase. The aforementioned results prove the feasibility of the modulation strategy through the combination of RE^{3+} and Zr^{4+} ions.

Supplementary Table 1. The eutectoid reaction data from RE_2O_3-HfO_2 phase diagrams.

No.	RE_2O_3-HfO_2	T_e (°C)	C_{RE} (at. %)
11158	Eu_2O_3-HfO_2	~1750	~17.65
09299	Gd_2O_3-HfO_2	~1760	~12.44
09337	Tb_2O_3-HfO_2	~1760	~11.98
09289	Dy_2O_3-HfO_2	~1770	~12.10
09302	Ho_2O_3-HfO_2	~1770	~11.16
09293	Er_2O_3-HfO_2	~1780	~10.17
09339	Tm_2O_3-HfO_2	~1780	~9.83
09344	Y_2O_3-HfO_2	~1770	~10.34
09359	Yb_2O_3-HfO_2	~1780	~11.52
09314	Lu_2O_3-HfO_2	~1780	~9.18
09325	Sc_2O_3-HfO_2	~1450	~17.48

Note: T_e is the eutectoid reaction temperature from the tetragonal phase, and C_{RE} is the key concentration of RE^{3+} ions avoiding the related eutectoid reaction.

Supplementary Table 2. Performance comparison of remanent polarization P_r in the HfO_2-based thin films and bulk crystals.

Materials	State/Thickness/Method	P_r ($\mu C/cm^2$)	Ref.
HfO_2	Film, 6.9 nm, ALD	13.5	Appl. Phys. Lett. 110, 022903 (2017)
Y:HfO_2 (5 at. %)	Film, 9-10 nm, PLD	50	Nat. Mater. 21, 903-909 (2022)
Si:HfO_2 (4.4 at. %)	Film, 8 nm, PLD	42	Acta Mater. 207,116696 (2021)
Si:HfO_2 (5.6 at. %)	Film, ~10 nm, ALD	~25	Adv. Mater. 26, 8198-8202 (2014)
La:HfO_2 (5.5 at. %)	Film, 10 nm, ALD	23	Appl. Phys. Lett. 114, 102903 (2019)
Y:HfO_2 (3.8 at. %)	Film, 20 nm, ALD	12.6	IEEE Electron Device Lett. 39, 823-826 (2018)
Gd:HfO_2 (2 at. %)	Film, 10 nm, ALD	12	ECS J. Solid State Sci. Technol. 1, N123 (2012)
Lu:HfO_2 (5 at. %)	Film, 10-40 nm, PLD	11	Appl. Phys. Lett. 111, 142904 (2017)
$Hf_{0.5}Zr_{0.5}O_2$	Film, ~10 nm, ALD	32	Front. Mater. 9, 969188 (2022)
$Hf_{0.5}Zr_{0.5}O_2$	Film, 5 nm, PLD	34	Nat. Mater. 17, 1095-1100 (2018)
$Hf_{0.5}Zr_{0.5}O_2$	Film, 15 nm, ALD	29	J. Mater. Sci. Technol. 104, 1-7(2022)
$Hf_{0.5}Zr_{0.5}O_2$	Film, 10 nm, ALD	26	Appl. Phys. Lett. 111, 242901 (2017)
$Hf_{0.5}Zr_{0.5}O_2$	Film, 10 nm, ALD	25	ACS Appl. Mater. Interfaces 14, 42232-42244 (2022)
$Hf_{0.5}Zr_{0.5}O_2$	Film, 75 nm, RF	21	Mater. Today Nano 22, 100320 (2023)
$Hf_{0.5}Zr_{0.5}O_2$	Film, 8 nm, PLD	~21	Nat. Commun. 14, 1780 (2023)
$Hf_{0.5}Zr_{0.5}O_2$	Film, ~10 nm, ALD	21	Nano Res. 15(4), 2913-2918 (2022)
$Hf_{0.5}Zr_{0.5}O_2$	Film, 15 nm, ALD	~21	Adv. Funct. Mater. 32, 2209604 (2022)
$Hf_{0.5}Zr_{0.5}O_2$	Film, 8 nm, ALD	~16	DOI: 10.1016/j.jmat.2023.05.010
$Hf_{0.5}Zr_{0.5}O_2$	Film, 10 nm, ALD	20.2	IEEE Electr. Device Lett. 43, 1235-1238 (2022)
$Hf_{0.5}Zr_{0.5}O_2$	Film, 10 nm, ALD	17.9	IEEE Electr. Device Lett. 43, 561-564 (2022)
$Hf_{0.5}Zr_{0.5}O_2$	Film, 10 nm, ALD	~17	ACS Appl. Mater. Interfaces 10, 8818-8826 (2018)
$Hf_{0.5}Zr_{0.5}O_2$	Film, 7.5-9.5 nm, ALD	16	Appl. Phys. Lett. 99, 112901 (2011)
$Hf_{0.25}Zr_{0.75}O_2$	Film, 10 nm, ALD	31	IEEE T. Electron Dev. 68, 1996-2002 (2021)
$Hf_{0.5}Zr_{0.5}O_2$	Film,10 nm, PLD	~7.5	Science 376, 731-738 (2022)
$Hf(Zr)_{1+x}O_2$ (x~0.2)	Film, 12 nm, Ion beam sputtering.	22	Science 381, 558-563 (2023)
La:$Hf_{0.5}Zr_{0.5}O_2$ (0.7 at. %)	Film, 10 nm, ALD	31	J. Appl. Phys. 125, 034101 (2019)

La:$Hf_{0.5}Zr_{0.5}O_2$ (1 at. %)	Film, 4.5-13 nm, PLD	35	ACS Appl. Electron. Mater. 2, 3221-3232 (2020)
La:$Hf_{0.5}Zr_{0.5}O_2$ (1 at. %)	Film, ~9nm, PLD	~28	Appl. Mater. Today 29, 101661 (2022)
Y:$Hf_{0.5}Zr_{0.5}O_2$ (5 at. %)	Film, ~40 nm, Solution	21	Jpn. J. Appl. Phys. 59, SMMB02 (2020)
Y:HfO_2 (7 at. %)	Film, 10-930 nm, PLD	~17	Appl. Phys. Lett. 115, 032901 (2019)
Y:HfO_2 (12 at. %)	Bulk, 2.7 μm, LDFZ	3	Nat. Mater. 20, 826-832 (2021)
Lu:$Hf_{0.6}Zr_{0.4}O_2$ (9.25 at. %)	Bulk, 17 μm, OFZ	26	This work

Note: ALD denotes atomic layer deposition, PLD represents pulsed laser deposition, RF corresponds to radio-frequency sputtering, LDFZ represents laser-diode-heated floating zone, and OFZ denotes optical floating zone.